RESEARCH ARTICLE | OCTOBER 09 2023

Picosecond pulsed 532 nm laser system for roughening and secondary electron yield reduction of inner surfaces of up to 15 m long tubes

Elena Bez ✉ 📵 ; Marcel Himmerlich 📵 ; Benoit Beaudou 📵 ; Ana Karen Reascos Portilla 📵 ;
Stefan Wackerow 📵 ; Martino Rimoldi 📵 ; Stephan Pfeiffer 📵 ; Markus Wiesendanger 📵 ; Fetah Benabid;
Mauro Taborelli 📵 ; Amin Abdolvand 📵 ; Paolo Chiggiato 📵

Check for updates

CrossMark

View Online

Export Citation

AIP Publishing

Picosecond pulsed 532 nm laser system for roughening and secondary electron yield reduction of inner surfaces of up to 15 m long tubes

View Online   Export Citation   CrossMark

Elena Bez,[1,2,a)]   Marcel Himmerlich,[1]   Benoit Beaudou,[3]   Ana Karen Reascos Portilla,[1]   Stefan Wackerow,[4]   Martino Rimoldi,[1]   Stephan Pfeiffer,[1]   Markus Wiesendanger,[5]   Fetah Benabid,[3]   Mauro Taborelli,[1]   Amin Abdolvand,[4]   and Paolo Chiggiato[1]

AFFILIATIONS

[1] CERN, European Organization for Nuclear Research, 1211 Geneva 23, Switzerland
[2] University of Leipzig, Linnéstraße 5, 04103 Leipzig, Germany
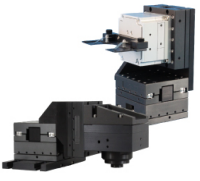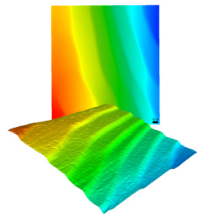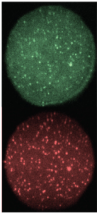[3] GLOphotonics SAS, 123 Avenue Albert Thomas, 87000 Limoges, France
[4] School of Science and Engineering, University of Dundee, Dundee DD1 4HN, Scotland
[5] Waygate Technologies Robotics, Technoparkstrasse 1, 8005 Zürich, Switzerland

[a)] Author to whom correspondence should be addressed: elena.annelie.bez@cern.ch

ABSTRACT

Laser-induced surface structuring is a promising method to suppress electron mulitpacting in the vacuum pipes of particle accelerators. Electrons are scattered inside the rough surface structure, resulting in a low Secondary Electron Yield (SEY) of the material. However, laser processing of internal pipe surfaces with a large aspect ratio is technologically challenging in terms of laser beam guidance and focusing. We present a 532 nm ultrashort-pulse laser setup to process the inner parts of 15 m long beam vacuum tubes of the Large Hadron Collider (LHC). Picosecond pulses at a repetition rate of 200 kHz are guided through an optical fiber toward an inchworm robot traveling inside the beam pipe. The system was installed, characterized, and tested for reliability. First surface treatments achieved the required scan precision. Cu_2O-dominated nano-features were observed when processing at high average laser power (5 W) and slow scanning speed (5 mm s^{-1}) in nitrogen flow, and the maximum SEY of copper was decreased from 2.1 to 0.7.

I. INTRODUCTION

Ultrashort-pulse laser processing allows for both fast and precise texturing of surfaces and objects, typically seeking low-reflectivity, high-emissivity,[1,2] or surfaces with defined wetting properties.[3–6] With the rapidly evolving laser technology, higher peak powers, shorter pulse lengths, and higher repetition rates are being achieved, enabling high efficiency and large-scale processing.

These processes are well developed on planar surfaces. However, there is a growing interest in three-dimensional (3D) laser processing of objects with peculiar shapes for industrial or scientific applications, such as laser-based cleaning of artworks,[7,8] laser milling,[9] or laser-texturing.[10–12] The challenge here is to access all regions of the target and to irradiate them at an optimum focused laser fluence, which ideally requires normal incidence of the laser beam and adjustable focusing.[13,14] Thereby, either the object itself or the laser beam must be guided. Three-dimensional laser measurement systems are being conventionally used to acquire the workpiece geometry and to adjust the focal distance accordingly.[15] To overcome the focal adjustment complexity, large Rayleigh lengths or diffractive elements have been used to enlarge the focal depth of the system or to divide the object into multiple subregions of low curvature.[12,16,17] Moreover, multi-axial or robot-assisted scanners are needed to access an object universally.[8]

03 November 2023 19:00:51

Particularly challenging is the processing of internal surfaces of an assembled and fixed object due to the restricted access, the associated spatial hindrance of the laser optics, and the fact that the object cannot be rotated. This rises the need for a beam delivery from the laser source to the target surface using for instance optical fibers.[18] In this study, a laser treatment of the internal parts of beam pipe tubes (beam screens) of the Large Hadron Collider (LHC) of 0.06 m in approximate diameter and a length of up to 15 m is targeted. The treatment is intended to suppress an electron cloud build-up in the vacuum tubes during accelerator operation, which can negatively impact its performance.[19–21] The laser-induced surface roughening reduces the SEY of the surface,[22–25] which is the amount of secondary electrons that are generated per incident electron. Consequently, secondary electron multiplicating in the LHC during beam circulation can be suppressed.[26] Starting in 2029, the LHC is expected to operate at higher luminosity[27] and the electron cloud density is expected to reach unacceptable values in certain areas of the machine. Therefore, the beam screens (BSs) of selected LHC units need surface treatment. However, they are installed inside dipole or quadrupole magnet assemblies that comprise a cryogenic cooling system and a complex vacuum system. The removal and replacement of the beam screens is an elaborate and time consuming operation, and in some cases, these magnets are unique. This high risk operation must be avoided, and a solution for an *in situ* treatment is required.

The beam screens are made of stainless steel, and a 75 μm thick copper layer is laminated onto the inner side. The tube consists of two opposed curved surfaces and two flat parts with a "hippodrome-like" cross section, thus ideally requiring a laser treatment at variable focal operation distance. Additionally, the distance between the flat parts is only ~61 mm. The small aperture together with the length of up to 15 m makes the beam delivery from the laser source to the target surface complex. Until now, no industrial solution is available to process such an object. Considering the length of the object, processing is likely to take several days or weeks, during which the whole system must operate stably, and especially, the optical system must be in thermal equilibrium. To obtain a laser-textured Cu surface that efficiently reduces the SEY, our previous study revealed that an average laser power of ~2 to 5 W at accumulated laser fluences of 100–1000 J cm^{-2} is necessary.[25] The surface structures must not be highly precise, but a distance of 50 $\pm$ 5 μm between the individual scan lines would ensure a homogeneous treatment.

Herein, we present the developed laser surface treatment setup that meets all the mentioned requirements. The system includes a hollow-core photonic crystal fiber for 532 nm ultrashort laser pulses combined with a beam delivery system and robot-assisted beam scanning. The setup was characterized and tested for reliability, and surface treatments were performed and analyzed by Scanning Electron Microscopy (SEM), X-ray Photoelectron Spectroscopy (XPS), and SEY measurements.

II. INSTRUMENTATION OF THE LASER TREATMENT SETUP

A. Experimental setup overview and optical components

An overview of the laser treatment setup is shown in Figs. 1 and 2. The aim is to imprint micro- and nanostructures on the
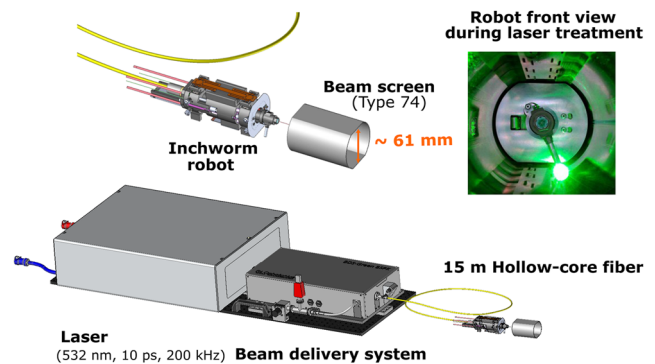

FIG. 1. In-situ laser treatment setup composed of a 532 nm laser source (Coherent HyperRapid NX), a beam delivery system (GLOphotonics), a 15 m hollow-core photonic crystal fiber (GLOphotonics), and a robot (Waygate Technologies Robotics) that travels inside the beam screen and irradiates the inner copper surface.

copper surface of the BS. Therefore, an ultrashort-pulse laser source (20 W, 10 ps, and 200 kHz) with a wavelength of λ = 532 nm, at which copper has a high absorption (~50%), was chosen to increase the ablation efficiency. A beam delivery system (BDS) was installed after the laser source in which the power (P_{BDS}) is regulated by an attenuator composed of a half-wave plate (HWP), which allows for selective rotation of the light polarisation axis, and a fixed thin film polarizer, which then filters out that part of the light that is not aligned with the polarizer axis. The 5 mm beam diameter of the laser source is shaped and focused into a 15 m long hollow-core photonic crystal fiber (HCPCF) to a mode field diameter MFD of

$$\text{MFD} = 2\sqrt{A_{\text{eff}}/\pi} = 26.4\,\mu m \tag{1}$$

using the approximation of the effective area $A_{\text{eff}} \cong 0.482\,\pi\,R_{\text{core}}^2$ with the core radius R_{core} of the hollow space enclosed by the ring of tubes and $R_{\text{core}}/\lambda > 27$ as previously proposed.[28]

The HCPCF guides the laser pulses to the inner surface of the beam screen via inhibited coupling (IC).[29] Since an ultrashort pulse laser is used, a solid silica fiber was not suitable due to changes in pulse characteristics (spectrum broadening and pulse duration) and degradation of the beam transmission properties (damage and intensity losses along the fiber),[29–31] both affecting the quality of the processed material (different laser–matter interaction).[32] The HCPCF is an eight-tube single ring fiber [Fig. 3(a)] with a hollow-core diameter of $2R_{\text{core}}$ = 38 μm. The coupling into such a small core diameter is sensitive to thermal fluctuations, which can occur during long operations (over days/weeks). They are stabilized by water cooling the critical components for light coupling and by correcting beam pointing drifts via piezo-actuated mirrors in the BDS, which compensate the beam position offsets measured by using two four-quadrant photodiodes. The hollow-core of the fiber is evacuated first via a turbomolecular pump and operated under static vacuum at a base pressure of about 2 mbar. Taking into account the laser peak power and the fiber length, the latter is evacuated to prevent the occurrence of optical non-linearities that are detrimental to the
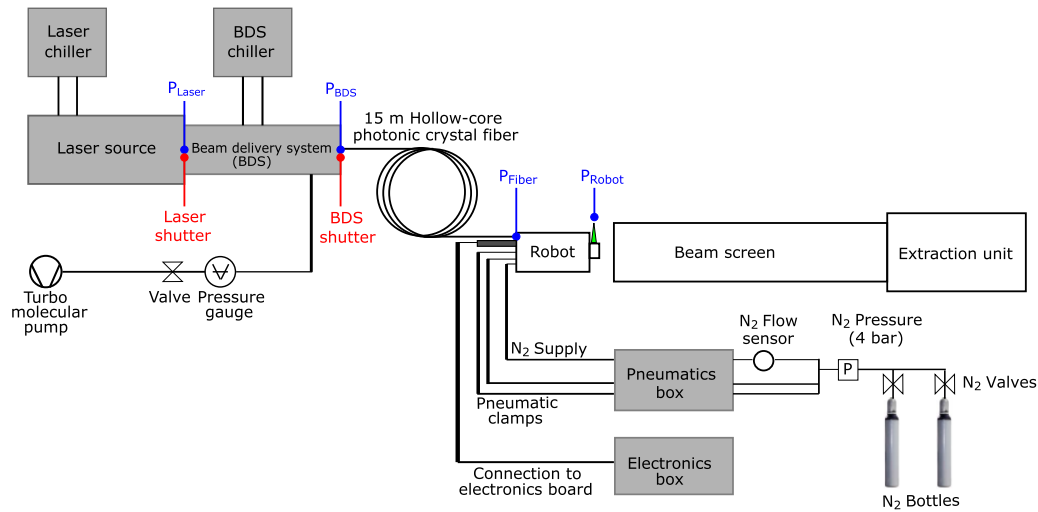
FIG. 2. Schematic overview of the complete laser treatment setup, including control, surveillance, and supply components. The locations of light power measurements are indicated in blue.
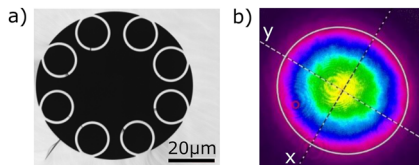
FIG. 3. (a) Cross-sectional photograph of the hollow-core tubular fiber with eight capillaries and the evacuated hollow-core (black part). (b) Collimated laser spot profile ($2\omega_{px} = 1.45$ mm, $2\omega_{py} = 1.6$ mm) at the fiber output cell.

pneumatics box and pressure sensors, the flow ($\sim$L min^{-1}) is controlled with a flowmeter installed upstream the pneumatics box, and the robot is connected to an electronics box (Fig. 2). During laser treatment tests in the laboratory, the beam screen is inserted into a

temporal and spectral shape of the pulse. The fiber is coiled up to a bending radius of 15 cm, as required for cable management of the targeted *in situ* treatment.

At the HCPCF output cell, the beam is first widened and then collimated to a spot diameter of $2\omega_p = 1.5$ mm with >90 % ellipticity [Fig. 3(b)].

The fiber is then inserted into a robot where the beam is focused by a plano-convex lens ($f = 90$ mm) and then deflected by a 45° oriented mirror inside a motorized rotating unit and directed toward the beam screen surface through a hollow tube that acts as nozzle for out-streaming nitrogen gas to minimize both oxidation of the copper beam screen surface and contamination of the optics in the internal part of the robot. This component rotates at defined speed to perform the treatment (Figs. 1 and 4).

The robot is designed to scan the laser beam across the surface by crawling [supported by nitrogen actuated clamps ($\sim$4 bar)] inside the beam screen, whose aperture is as small as 61 mm (Fig. 1, top left). Moreover, it can be adapted to smaller beam screen geometries, such as those installed in arc dipole magnets of the LHC (BS type 50 A: radial diameter 46.35 mm, distance between flat parts 36.75 mm).[33]

The gas supply for both the pneumatic clamps and the flow through the nozzle is controlled via fast-switching valves in the

FIG. 4. (a) Side-view photograph of the robot. (b) Cross-sectional 3D model of internal parts of the robot. (c) Schematic of laser beam collimation at fiber output cell and beam focusing in the robot.

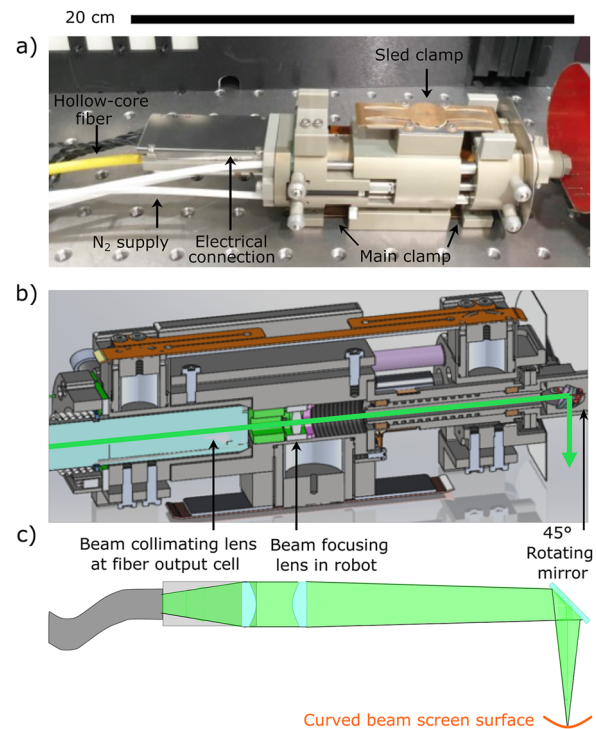tube for laser safety reasons and a vacuum-based extractor (Weller Laser Line LL 200 V) creates a continuous air-flow that removes the particles and dust expelled from the surface during laser ablation and stores them in a filter unit. All devices, including the robot, were integrated into an embedded real-time industrial controller (Compact Rio) from National Instruments combined with a customized user interface in LabVIEW. During a treatment, the laser shutter is permanently open and the laser scanning is controlled via actuating the shutter in the BDS. A more detailed description of the software integration can be found elsewhere.[34]

B. Robot-assisted scanning

The robot [Fig. 4(a)] uses coarse longitudinal motion to move forward in the beam screen between treatments and a fine longitudinal motion to move its laser scan arm during treatments. The sled is connected to the main body by a linear rail and a precision spindle (pitch 1 mm). This allows for accurate position control in the linear axis. The coarse step is supported by pneumatic clamps on the upper part of the sled (sled clamp) and on the lower part of the main body (main clamp) that are actuated by pressurized nitrogen (~4 bar). Thus, the robot performs an inchworm movement by alternately actuating the clamps and linearly advancing the body/sled. The robot head, where the laser beam is directed onto the surface, rotates via intermeshing gears and a pinion. Both rotary and translational axes are driven by brushless DC motors. A magnetic quadrature encoder converts the electronic signals of the motor into counts: 4096 cts/mm on the linear axis and 32 768 cts/rev on the rotational axis. This results in a spatial resolution of 0.24 μm (translation) and 0.011 degree (rotation) or 0.62 μm on the beam screen surface, respectively.

The theoretical motor top speed is limited by the available voltage (24 V). For the surface treatment, it translates into a maximum rotational scanning speed (defined along the scan line and relative to the beam screen surface) of ~200 mm s^{-1} and a maximum translational speed of ~50 mm s^{-1}, which corresponds to a minimum processing time of 0.6 s cm^{-2} and 2.3 s cm^{-2} respectively for a line distance of 50 μm. However, the actual processing time is longer because readjusting the clamps of the robot requires additional time.
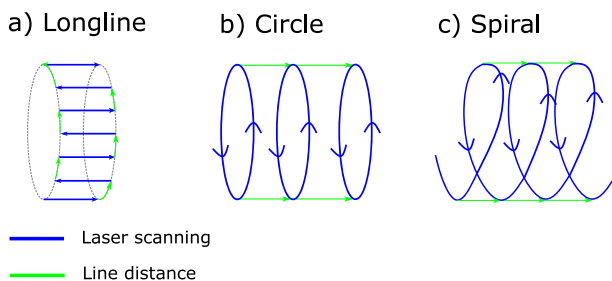

FIG. 5. Implemented scan patterns that are executed by the robot. During laser line scanning (blue), the BDS shutter is open and closed when moving to the next line (a, b), and always open during the spiral (c). The line distance (green) is defined by a rotational step for the longline movement (a) and by a linear move of the robot for circular (b) and spiral movement (c).

By combining the linear and rotational motion, a selection of scanning patterns for surface processing have been implemented and tested (Fig. 5): (a) a longitudinal line movement (longline), where the line spacing is defined by a rotational step; (b) a circular movement, where the laser beam is rotated azimuthally and the line distance is defined by a (fine) linear forward translation; and (c) a spiral movement, which is a combination of azimuthal rotation and a continuous (fine) linear forward movement of the body whose velocity is adapted to the rotation speed, the geometry of the beam screen, and the line spacing.

III. CHARACTERIZATION OF THE SETUP

A. Power transmission and stability

Four points (Fig. 2) of the system are relevant for monitoring the laser light power: at the laser source output (P$_{Laser}$), at the output of the BDS before the beam injection in the fiber (P$_{BDS}$), at the fiber output cell (P$_{Fiber}$), and at the robot head (P$_{Robot}$). The laser source provides an average laser output power of up to P$_{Laser}$ = 20 W, which was restricted to 11 W to avoid any degradation or local damage of the fiber. Since the power P$_{BDS}$ that is injected in the HCPCF is not measured continuously, it was beforehand calibrated for different HWP angular positions. The measurement was fitted using Malus law[35] to characterize the power reduction by the combination of HWP and the linear polarizer [Fig. 6(a), fit parameters included],

$$\frac{P_{BDS}}{P_{Laser}} = y_0 + A \cdot \cos^2\left(\frac{2\pi}{360°}\left(B \cdot \alpha - \alpha_0\right)\right), \quad (2)$$

where α corresponds to the HWP angle. $\alpha_0 = 1.293°$ is the alignment angle relative to the beam position; $B = 1.992$ is the periodicity of the HWP, which is close to ideally 2; $A = 96.353\%$ is the maximum of transmitted intensity, implying <4% losses due to reflections/absorption on the optical components; and $y_0 = 0.189\%$ represents the transmitted intensity when the polarization direction behind the HWP is perpendicular to the polarizer axis. These numbers correspond to an extinction ratio of ~1:510 for the component, which is sufficient for the application for power regulation in the intermediate range.

The average laser power at the fiber output P$_{Fiber}$ is not recorded permanently during processing in the beam screens due to the limited spatial access. It is, therefore, measured manually with an external thermal power sensor before and after laser processing. An overview of the measured power values is shown in Fig. 6(b). The transmission of the fiber T$_{Fiber}$ = P$_{Fiber}$/P$_{BDS}$ amounts to ~70% (−1.3 dB) for low average input power (~1 W), while it decreases to ~50% (−3 dB) for higher average input power (~10 W).

The attenuation was measured [Fig. 6(c)] using a broadband source (supercontinuum from 300 to 1800 nm) at low power (<100 mW) to couple into the fiber and an Optical Spectrum Analyzer (OSA) to measure the output spectrum. The power difference was measured at both its full length and at a cut length of 3–5 m (cutback method) placed in a loose position (25 cm bending radius). At the wavelength of 532 nm, the attenuation amounted to 25 dB km^{-1}, which correlates with −0.375 dB (92% transmission) for a length of 15 m. Transmission losses in the setup are attributed to propagation losses (−0.375 dB), 85–96% coupling losses at the fiber injection (−0.7 to −0.2 dB), and bending losses of −1.1 dB (−0.02 to
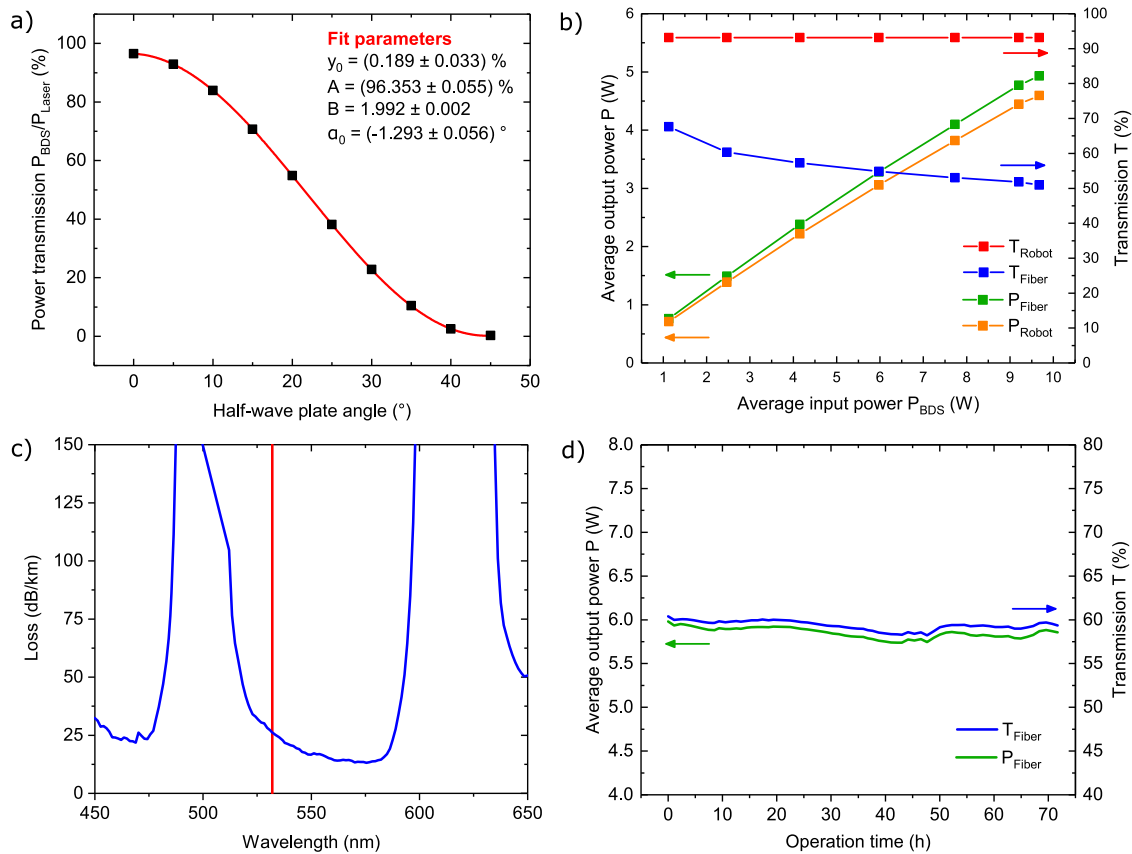
FIG. 6. (a) Measured (black) and fitted [red, according to Eq. (2)] transmitted laser power (%) through the attenuator in the BDS as a function of half-wave plate angle. (b) Power transmission through the 15 m long hollow-core fiber and through the robot for various input powers. T_{Fiber} determined at a later stage than for (d), i.e., after several weeks of operation. As discussed, it can decrease over time due to degradation. (c) Attenuation of the 15 m HCPCF coiled to a bending radius of 25 cm in the spectral range of 450–650 nm, measured by the cutback method. The wavelength of 532 nm (used in the setup) is indicated by the red vertical line. (d) Long-term power stability test over 70 h. The average laser power at the fiber output cell was measured using an external power sensor.

−0.05 dB/turn for a radius of curvature 11 cm) if the fiber is coiled along its full length. In sum, this results in an overall loss of about −1.675 dB, corresponding to a transmission of 68%.

Bending losses have, therefore, a major impact on the transmission quality. The fabrication of HCPCF for short wavelength remains challenging due to the difficulty in maintaining a thin, homogeneous microstructure along the fiber during the drawing process. Consequently, most of IC HCPCF guide short wavelengths in high-order transmission bands[29] that are spectrally narrower and require additional care in their relative position to the laser wavelength. The transmission band position of the BDS fiber is a balanced design between modal quality and bending sensitivity. The bending loss of the IC HCPCF is not constant over the entire transmission band. The bending affects the edge of the transmission band more than the central part. On the other hand, the loss ratio between the high order modes and the TEM_{00} fundamental mode increases at the edge of the transmission window. The compromise found is to set the operating wavelength (532 nm) to the fifth quarter (wavelength-wise) of the transmission band [see Fig. 6(c)], which results in good

beam quality but rather bend-sensitive transmission of the fiber. The shorter the laser wavelength, the more difficult it becomes to fabricate HCPCFs because the core diameter of the fiber must be smaller to reduce Rayleigh scattering at the surface roughness of frozen-in capillary waves, which is the dominant loss factor at shorter wavelengths. These losses scale with a factor of $1/\lambda^3$.[36] Therefore, the fabrication method is crucial with respect to small and highly precise geometries. Since the core diameter must be rather small at short wavelengths, focusing the laser into the fiber and maintaining coupling over long periods of time are challenging. This combined with a length of 15 m and a bending radius of 15 cm explains the fiber transmission of about 60%. It has to be further noted that the losses caused by the optical components in the robot (lens, mirror, nozzle) are minor (5%) [Fig. 6(b)].

The setup was designed to perform large-scale surface treatments that can last several days or weeks. Therefore, the beam coupling must be reliable and robust to environmental variations in temperature and humidity without degrading the fiber to achieve a uniform laser treatment. A continuous measurement (at an early

03 November 2023 19:00:51

fiber use time stage) over 70 h [Fig. 6(d)] showed a stable transmission of about 60% and an average power at the fiber output of $P_{Fiber} = 5.9 \pm 0.1$ W. Fluctuations of 0.1 W or 2% of the nominal laser power will not result in SEY differences, especially when processing at higher accumulated laser fluences (~1000 J cm^{-2}), where a saturation of the SEY maximum was observed.[25]

B. Laser spot properties at the beam screen surface

The theoretical Gaussian laser diameter $2\omega_0$ in the focal point at the exit of the robot is calculated to be

$$2\,\omega_0 = 2\,\frac{\lambda f M^2}{\pi \omega_p} = 52.8\,\mu m, \tag{3}$$

with a beam quality factor $M^2 \leq 1.3$, and the Rayleigh length is calculated to be

$$z_R = \frac{\pi \omega_0^2}{\lambda M^2} = 3.2 \text{ mm.} \tag{4}$$

The relatively large Rayleigh length provides a focal depth of $z_0 = 2z_R = 6.4$ mm.

Setting the focal point on the curved part of the hippodrome-shaped beam screen results in a defocused beam on the flat part, as indicated in Fig. 7(a). The offset between the closest and the furthest part is 4.85 mm. At 4.85 mm defocus, the theoretical peak intensity of the Gaussian laser beam reduces to ~30%. Explicitly, the peak fluence has dropped from 2.28 to 0.68 J cm^{-2} for an average power of 5 W [Fig. 7(b)] and the spot size widens to

$$2\,\omega\,(z = 4.85 \text{ mm}) = 2\left(\omega_0\,\sqrt{1 + \left(\frac{z}{z_R}\right)^2}\right)$$
$$= 96.6\,\mu m. \tag{5}$$

The available laser fluence on the curved part provides enough flexibility to create structures that reduce the SEY on the copper surface.[25,37] The laser fluence on the flat part remains above the ablation threshold of copper (~0.24 J cm^{-2}),[23] enabling surface modification. Increasing the number of pulses per surface area (e.g., slower scanning) can compensate for a lower intensity.[24] The differences in fluence could be adjusted by moving the focal point to a distance between the curved and the flat part so that both surfaces are slightly defocused, but resulting in a more homogeneous surface treatment, if required. However, the lens in the robot is mounted in a screw-in housing and cannot be moved during processing, i.e., no automatic focus corrections are applied.

The laser spot diameter was experimentally evaluated using Liu's method.[38] To do so, laser lines of various average power P were engraved on the curved surface whose spatial profile approximately reflects a Gauss function. The widths D of the trenches, where material was ablated, were measured from 2D profiles [example in Fig. 8(a)] acquired with a white light interferometer (Veeco Nt3300). Assuming a Gaussian spatial beam profile, the relation between the trench width D and the laser power P can be written as[38]

$$D^2 = 2\,\omega_0^2\,\ln\left(\frac{P}{P_0}\right), \tag{6}$$

with P_0 being the threshold laser power for material ablation.
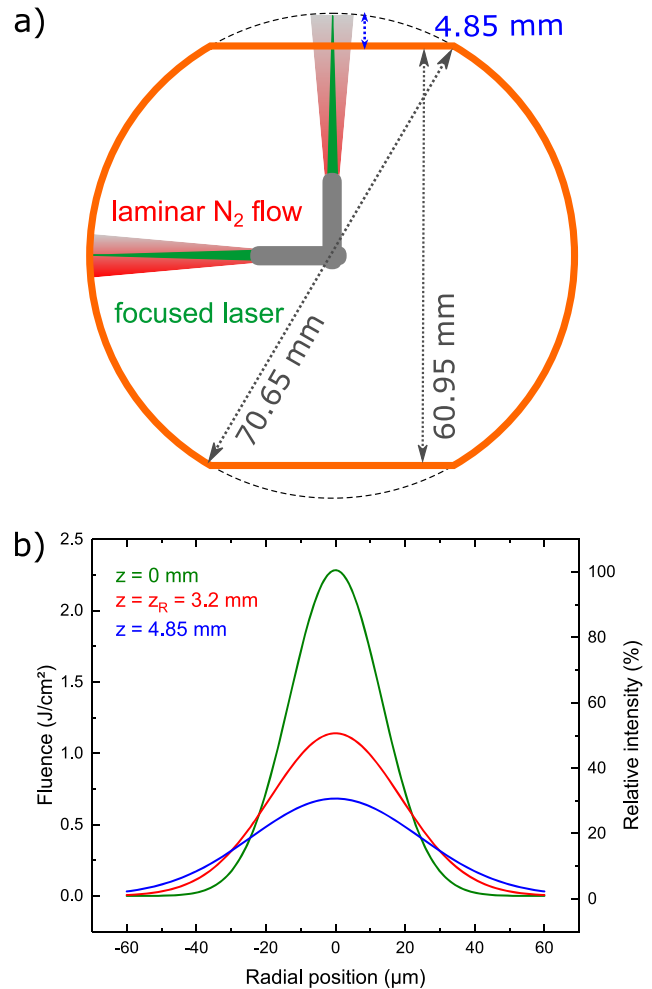
FIG. 7. (a) Cross-sectional illustration of the beam screen hippodrome geometry, laminar gas flow though the nozzle of the robot, and the focal point position are indicated. Dimensions of the beam screen (type 74) and the offset between the flat and the curved part are highlighted (in blue). (b) Calculated fluence distribution for an average laser power of 5 W in the focal point (green), at the Rayleigh length (red), and at the offset of the curved and the flat part of the beam screen (blue).

From the slope of the plot in Fig. 8(b), the Gaussian diameter (defined at the width where the photon intensity has fallen to $1/e^2$) is

$$2\,\omega_0 = 61.7\,\mu m. \tag{7}$$

Deviations to the theoretical value [Eq. (3)] may occur if the beam at the fiber output was not perfectly collimated (smaller ω_p) or if the lens in the robot was slightly misaligned.

C. Scan precision

The implemented scan patterns (Fig. 5) were tested for precision on curved copper samples (see processing details in Sec. IV). For this, each scan line should be separated by $50 \pm 5\,\mu m$ to generate homogeneous surface structures.

03 November 2023 19:00:51

a)

b)

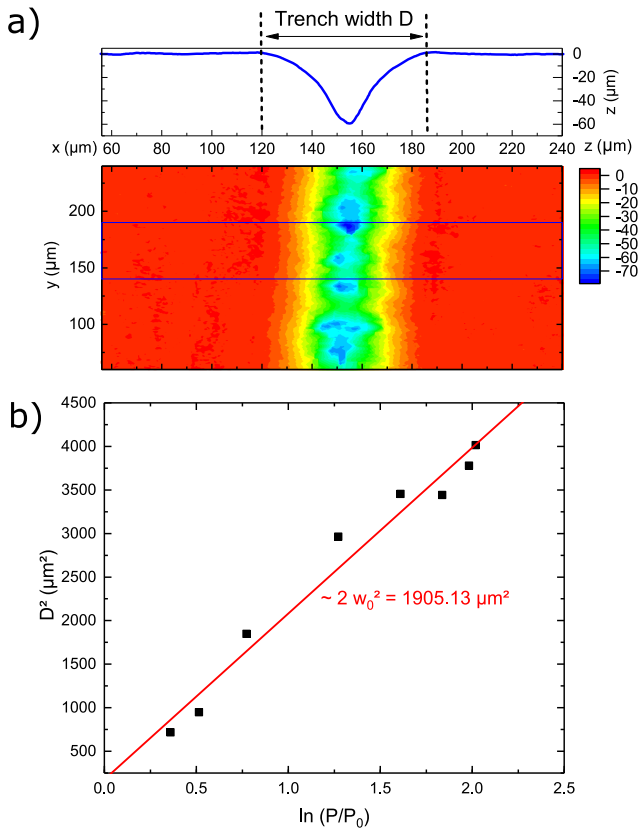**FIG. 8.** (a) Trench width and depth profile (averaged over blue marked range) engraved at P = 3.1 W and v = 5 mm s^{-1} as measured by white light interferometry. (b) Laser diameter evaluation at the curved beam screen surface using Liu's method.[38]

FIG. 9. Cross-sectional optical microscopy images (left column) and SEM images of micrometer trenches oriented in the laser scanning direction (right column). Laser-processed copper samples using (a) longline, (b) circular, and (c) spiral movement at a nominal line distance of $\Delta y = 50$ μm, a N_2 flow rate of 4 L min^{-1}, an average laser power of $P_{Robot} = 4$ W, and scanning speeds of (a) 5 mm s^{-1}, (b) 15 mm s^{-1}, and (c) 15 mm s^{-1}, equivalent to accumulated laser fluences of (a) 1600 J cm^{-2}, (b) 530 J cm^{-2}, and (c) 530 J cm^{-2}. The sample preparation for the material characterization and the used experimental equipment are described in detail in Ref. [25].

The ultrashort laser pulses ablated the copper surface and resulted in micrometer deep trenches oriented in the laser scanning direction. From a cross-sectional view (samples were laterally polished and ground), the distances between each minimum of the trenches were measured with an optical microscope at five different points along the cross section (Fig. 9, left column). The average distances amounted to 50.0 ± 3.6 μm for longline (a), 48.0 ± 3.6 μm for the circle (b), and 49.3 ± 3 μm for the spiral movement, which confirms the precision of the robot movement in both the translational and rotational axis. A deviation of ~3 μm for the different actuation procedures is acceptable for the intended large-scale surface roughening and could be minimized calibrating the control software settings, if required.

It has to be pointed out that trenches oriented perpendicular to the beam propagation direction in the LHC cause a higher increase of the surface resistance compared to longitudinally aligned trenches,[39] deteriorating the beam quality and adding a contribution to the heat load on the cryogenic system, which would overcome its capacity. Therefore, surface structures, which are created using the longline movement, can be beneficial to keep the surface resistance low.
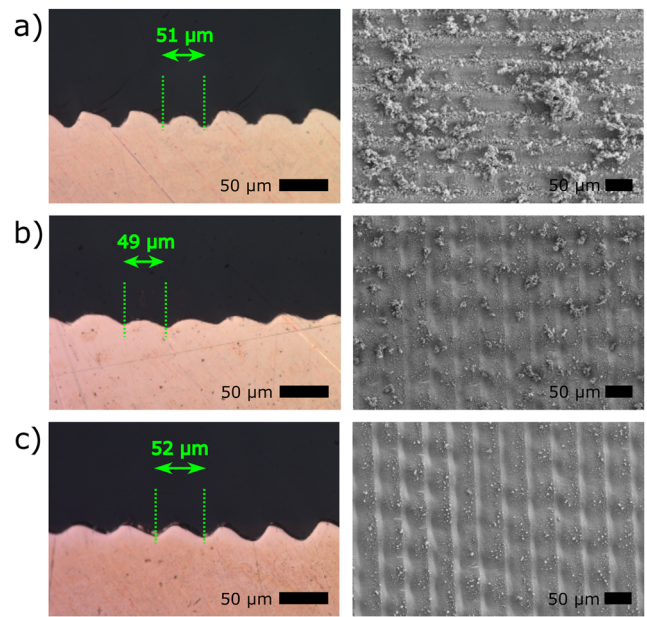
IV. LASER PROCESSING: SURFACE PROPERTIES

Laser processing tests were performed on 12 × 15 mm^2 oxygen-free, curved copper samples that were inserted at the curved part of the beam screen so that the inner surfaces are flush. Before processing, the samples were etched (HCl), wet-chemically degreased with a commercial detergent, rinsed in de-ionized water, and passivated with chromic acid. The laser focus was set to match the surface of the curved beam screen region, and an average power of $P_{Robot} = 4$–5 W, a line distance of $\Delta y = 50$ μm, a scanning speed of v = 5 mm s^{-1}, and a N_2 flow rate of 4 L/min were applied.

The ps laser pulses engrave micrometer deep trenches in the copper surface that are covered with nanometer-sized structures (Figs. 9 and 10). Note that the trenches in Fig. 9 are less pronounced and covered with less particles compared to Fig. 10 because lower fluences (1600, 530 J cm^{-2}) were used, consistent with previous results.[25] The laser-processing in air (without additional flow through the nozzle), at high average laser power (5 W) and slow scanning speed (5 mm s^{-1}), which corresponds to an accumulated laser fluence of 2000 J cm^{-2}, resulted in typical cauliflower-head nanostructures.[24,25,37] Otherwise, when applying a local nitrogen flow through the nozzle of the robot, fine nanometer-sized molten and re-solidified spheres are created at the surface (Fig. 10). The application of the nitrogen flow is indispensable to protect the optics in the robot from being contaminated by particles. Furthermore, the
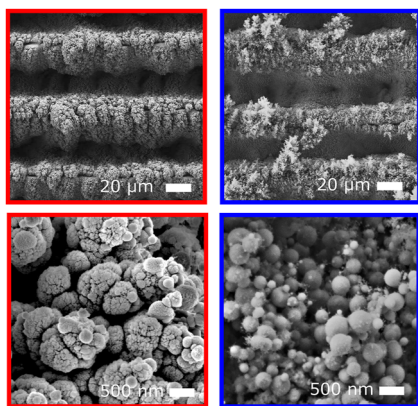
03 November 2023 19:00:51

FIG. 10. Scanning electron micrographs of micro- (top row) and nanostructures (bottom row) at the surface of laser-processed Cu in air (red) and local N_2 flow of 4 L min^{-1} (blue) at an average laser power of $P_{Robot} = 5$ W, a scanning speed of $v = 5$ mm s^{-1}, and a line distance of $\Delta y = 50$ μm, equivalent to an accumulated laser fluence of 2000 J cm^{-2}. The used experimental equipment and settings for sample characterization are described in detail in Ref. 25.

nitrogen stream confines the expanding plasma and pushes particles expelling from the ablation zone partially back to the surface. The redeposited particles tend to cluster on the formed trenches and create a surface topography that is more undefined than that resulting from processing in air without nitrogen flow. The gas flow dynamics could be improved in the future by modifying the nozzle design or adjusting the nitrogen flow. In addition, these redeposited spherical clusters are loosely bound to the surface and can be removed in a consecutive cleaning process.

The amount of gas flowing through the nozzle generates a local nitrogen atmosphere that limits particle oxidation in the plasma phase. This was confirmed by the performed XPS measurements, which had been carried out using the same experimental equipment (UHV system containing a hemispherical electron energy analyzer and a monochromated AlKα x-ray source [hν = 1486.7 eV] and settings (overall spectral resolution for the shown spectra is 0.7 eV (FWHM of Ag3d$_{5/2}$ sputter-cleaned polycrystalline Ag) as those reported in Ref. 25. Figure 11 shows that the processed surface was composed of Cu_2O since the Cu 2p$_{3/2}$ main state is at 932.4 eV binding energy (B.E.) and the Cu LMM Auger transition is at 916.7 eV kinetic energy (K.E.) (modified Auger parameter of 1849.1 eV). Furthermore, the presence of $Cu(OH)_2$ is indicated by the shoulder of the Cu 2p$_{3/2}$ state at 934.4 eV B.E. and by the shape of the Cu(II) satellite feature between 938 and 948 eV B.E.,[40–42] while no nitrogen was detected at the surface. The Cu_2O formation for treatment in nitrogen flow is comparable to previous studies, where the laser treatment was performed in the nitrogen or argon atmosphere.[43] However, nitrogen was incorporated in the surface and less copper hydroxide was detected for that earlier study, which could be linked to the difference in the way the nitrogen is supplied (flow of local N_2 stream vs processing in nitrogen environment).

When laser processing was performed in air, on the contrary, the ablated particles oxidized due to the interaction with the reactive species formed in the laser-induced plasma plume, resulting in a CuO-dominated surface. The Cu 2p$_{3/2}$ state is found at 933.7 eV B.E., the Cu LMM Auger transition is at 917.5 eV K.E. (modified Auger parameter of 1851.2 eV), and the O 1s peak is at B.E. 529.5 eV, which all point to the existence of CuO.[40,44,45] Considering the used processing parameters, these tendencies fit the observations of surface properties in earlier model studies that had been performed on flat samples[23,37,43] without the fiber and the robot, and the compositional surface transformations are an expected outcome for a laser processing in air.[25]

After laser-processing in air and nitrogen, the SEY of the samples was measured in an ultrahigh vacuum system at three different spots on each sample using the sample bias method.[46] Figure 12 compares the primary electron energy dependence of SEY (3-spot average) between 50 and 1800 eV for a degreased and passivated Cu sample and the two samples that had been either laser-treated in air or with the support of the nitrogen flux. A significant SEY reduction was found in the entire energy range, and the SEY maximum
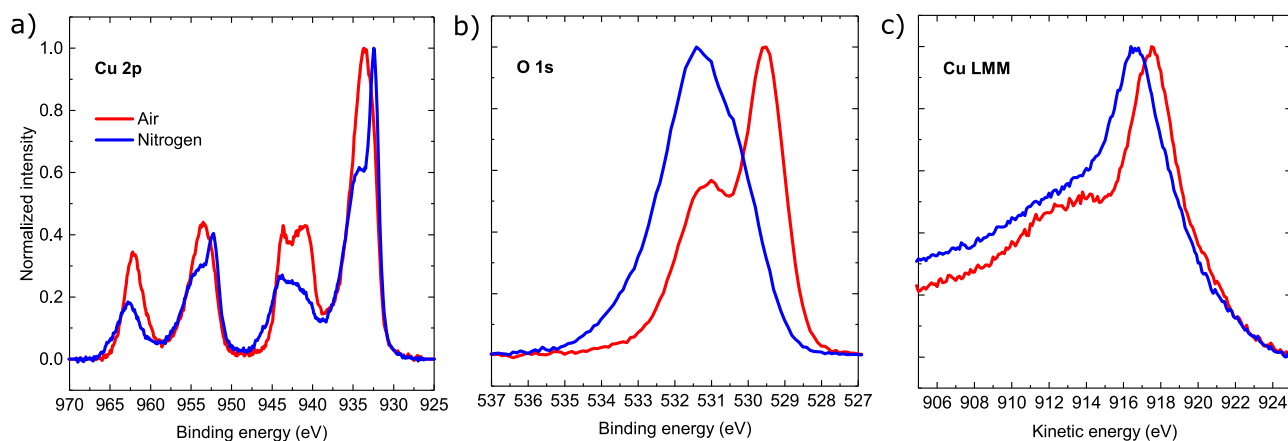
FIG. 11. XPS spectra of (a) Cu 2p state, (b) O 1s state, and (c) Cu LMM Auger excitation of laser-processed curved copper surfaces in air (red) and local nitrogen flow of 4 L/min (blue).
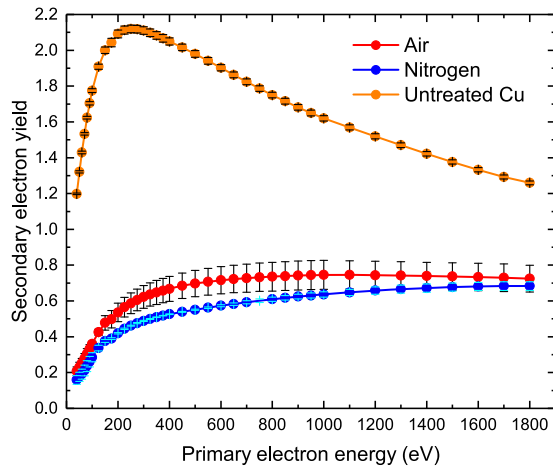
FIG. 12. Secondary electron yield of untreated (degreased) Cu (orange) and laser-processed Cu in air (red) or local nitrogen flow (blue) at an accumulated fluence of 2000 J cm^{-2}. The error bars indicate the standard deviation of the three-spot averaged curves.

decreased to 0.75 ± 0.06 (air) and 0.68 ± 0.01 (nitrogen) compared to the untreated copper surface, which had a SEY maximum of 2.1 at a primary electron energy of 250 eV. The generated micrometer trenches and nanostructures efficiently absorb the low energetic electrons (<500 eV), while a larger proportion of electrons with higher energy is backscattered from the surface, leading to a shift of the SEY maximum to higher kinetic energies.[23,25] The efficient absorption at low primary electron energies is advantageous for the application since the majority of electrons, which impinge on the inner beam screen surface in the LHC, have kinetic energies of up to 500 eV.[47] A small difference of the SEY in dependence of primary electron energy was found for the treatments in air and in nitrogen, only slightly above the relative experimental error of the measurement setup (0.05), and linked to the difference in surface topography (especially in the sub-micrometer scale—see Fig. 12) and surface composition (Fig. 11). The SEY difference between the two laser-treated samples is generally not significant for electron cloud mitigation, as both processes lead to SEY values well below unity. Nonetheless, the addition of N$_2$ to suppress CuO formation is beneficial to mitigate charging effects that could otherwise occur at cryogenic conditions.[43]

V. CONCLUSIONS

In the present study, an *in situ* solution to laser-treat inner surfaces of up to 15 m long tubes, without the need to move the object, is presented. The setup comprises a hollow-core fiber for guidance of 532 nm ultrashort pulses and a robot-assisted laser scanning. A 70 h-long performance test confirmed that the setup delivers a stable average output power of 5 W at 60% transmissivity of the entire optical system. The 532 nm wavelength was originally chosen to ensure high ablation efficiency on the copper target, but the HCPCF is better suited for longer wavelengths, for which a transmission of more than 90% can be achieved.[48] As an alternative, an infrared laser could be used to further improve the stability and efficiency of the

system. In a comparative study on a simpler test bench without a fiber and the robot, we have shown that similar SEY reduction can be achieved with a wavelength of 1064 nm.[25] In addition, a continuous power measurement at the fiber output or at the robot head would be beneficial for controlling the stability of the treatment. This will be implemented in a next step to better control the processing conditions, which requires a modification of the robot or the fiber output cell. Currently, the choice of a large Rayleigh length ensures that a sufficient laser power is available even when processing slightly out of focus. As an upgrade, the focusing lens in the robot could be combined with a diffractive optical element (DOE), which further increases the focal depth of the beam.[17]

First surface treatments showed the functionality of the system using various scanning techniques, with which the orientation of the trenches can be controlled. The laser surface treatment demonstrated that the SEY maximum can be reduced to 0.7, which is sufficient to suppress electron-cloud formation. Reducing the SEY of the surface is one of the major requirements for electron cloud mitigation in the LHC. The used parameters (average laser power 5 W, scanning speed 5 mm s^{-1}, and line distance 50 μm) correspond to a processing speed of 400 s cm^{-2}. However, the laser processing parameters can be optimized, for instance, by increasing the scanning speed or decreasing the accumulated laser fluence.[25] Until now, the system was used to treat short beam screen segments of 50 cm, and it is planned to perform treatments of up to several meters in accordance with the length of LHC magnets.

AUTHOR DECLARATIONS

Conflict of Interest

The authors have no conflicts to disclose.

Author Contributions

Elena Bez: Conceptualization (equal); Formal analysis (equal); Investigation (equal); Methodology (equal); Visualization (lead); Writing – original draft (lead). **Marcel Himmerlich**: Conceptualization (equal); Project administration (equal); Supervision (lead); Validation (equal); Writing – original draft (supporting); Writing – review & editing (equal). **Benoit Beaudou**: Investigation (equal); Methodology (equal); Resources (equal); Visualization (supporting);

03 November 2023 19:00:51

Writing – review & editing (equal). **Ana Karen Reascos Portilla**: Investigation (equal); Methodology (equal); Resources (equal); Writing – review & editing (equal). **Stefan Wackerow**: Methodology (equal); Resources (equal); Writing – review & editing (equal). **Martino Rimoldi**: Formal analysis (equal); Investigation (equal); Resources (equal); Writing – review & editing (equal). **Stephan Pfeiffer**: Formal analysis (equal); Investigation (equal); Writing – review & editing (equal). **Markus Wiesendanger**: Investigation (equal); Software (equal); Visualization (supporting); Writing – review & editing (equal). **Fetah Benabid**: Project administration (supporting); Writing – review & editing (equal). **Mauro Taborelli**: Conceptualization (equal); Project administration (equal); Supervision (supporting); Validation (equal); Writing – review & editing (equal). **Amin Abdolvand**: Funding acquisition (supporting); Writing – review & editing (equal). **Paolo Chiggiato**: Funding acquisition (lead); Writing – review & editing (equal).

DATA AVAILABILITY

The data that support the findings of this study are available from the corresponding author upon reasonable request.

REFERENCES

[1] A. Y. Vorobyev and C. Guo, "Reflection of femtosecond laser light in multipulse ablation of metals," J. Appl. Phys. **110**, 043102 (2011).

[2] G. Tang, A. C. Hourd, and A. Abdolvand, "Nanosecond pulsed laser blackening of copper," Appl. Phys. Lett. **101**, 231902 (2012).

[3] Z. Zhao, C. Wang, M. Li, and L. Wang, "Nd:YAG laser surface treatment of copper to improve the wettability of $Sn_{3.5}Ag$ solder on copper," Surf. Coat. **200**, 2181–2186 (2005).

[4] A. Y. Vorobyev and C. Guo, "Direct femtosecond laser surface nano/microstructuring and its applications," Laser Photonics Rev. **7**, 385–407 (2013).

[5] C. Deng and H. Ki, "Tunable wetting surfaces with interacting cavities via femtosecond laser patterning and wet etching," J. Appl. Phys. **128**, 015306 (2020).

[6] K. Yin, Z. Wu, J. Wu, Z. Zhu, F. Zhang, and J.-A. Duan, "Solar-driven thermal-wind synergistic effect on laser-textured superhydrophilic copper foam architectures for ultrahigh efficient vapor generation," Appl. Phys. Lett. **118**, 211905 (2021).

[7] A. J. López, J. Lamas, J. S. Pozo-Antonio, T. Rivas, and A. Ramil, "Development of processing strategies for 3D controlled laser ablation: Application to the cleaning of stonework surfaces," Opt. Lasers Eng. **126**, 105897 (2020).

[8] A. Rodríguez, A. J. López, J. Lamas, A. Moreno, and A. Ramil, "Robot-assisted laser ablation for 3D surfaces. application for paint removal with ultrashort pulse laser," Opt. Lasers Eng. **160**, 107284 (2023).

[9] G. Cuccolini, L. Orazi, and A. Fortunato, "5 axes computer aided laser milling," Opt. Lasers Eng. **51**, 749–760 (2013).

[10] A. Žemaitis, M. Gaidys, P. Gečys, G. Račiukaitis, and M. Gedvilas, "Rapid high-quality 3D micro-machining by optimised efficient ultrashort laser ablation," Opt. Lasers Eng. **114**, 83–89 (2019).

[11] B. Zheng, G. Zhao, Z. Yan, Y. Xie, and J. Lin, "Direct freeform laser fabrication of 3D conformable electronics," Adv. Funct. Mater. **33**, 2210084 (2023).

[12] X. Wang, J. Duan, M. Jiang, S. Ke, B. Wu, and X. Zeng, "Study of laser precision ablating texture patterns on large-scale freeform surface," Int. J. Adv. Manuf. Technol. **92**, 4571–4581 (2017).

[13] A. Michalek, A. Batal, S. Qi, P. Penchev, D. Bruneel, T. L. See, and S. Dimov, "Modelling ultrafast laser structuring/texturing of freeform surfaces," Appl. Surf. Sci. **2**, 100036 (2020).

[14] A. Garcia-Giron, J. Romano, A. Batal, A. Michałek, P. Penchev, and S. Dimov, "Experimental investigation of processing disturbances in laser surface patterning," Opt. Lasers Eng. **126**, 105900 (2020).

[15] J. Diaci, D. Bračun, A. Gorkič, and J. Možina, "Rapid and flexible laser marking and engraving of tilted and curved surfaces," Opt. Lasers Eng. **49**, 195–199 (2011).

[16] P. S. Salter and M. J. Booth, "Adaptive optics in laser processing," Light: Sci. Appl. **8**, 110 (2019).

[17] R. Uren, A. Din, S. Wackerow, E. Bez, S. Pfeiffer, M. Rimoldi, M. Himmerlich, M. Taborelli, and A. Abdolvand, "Out of focus ultrafast processing of metals for reduced secondary electron yield," Opt. Mater. Express **13**, 1228–1240 (2023).

[18] B. Debord, A. Amsanpally, M. Chafer, A. Baz, M. Maurel, J. M. Blondy, E. Hugonnot, F. Scol, L. Vincetti, F. Gérôme, and F. Benabid, "Ultralow transmission loss in inhibited-coupling guiding hollow fibers," Optica **4**, 209–217 (2017).

[19] O. Dominguez, K. Li, G. Arduini, E. Metral, G. Rumolo, F. Zimmermann, and H. M. Cuna, "First electron-cloud studies at the large hadron collider," Phys. Rev. Spec. Top.–Accel. Beams **16**, 011003 (2013).

[20] R. Cimino and T. Demma, "Electron cloud in accelerators," Int. J. Mod. Phys. A **29**, 1430023 (2014).

[21] G. Iadarola, B. Bradu, P. Dijkstal, L. Mether, G. Rumolo, G. Skripka, and L. Tavian, "Overview on heat loads in the LHC," in *Proceedings of the Joint INFN-CERN-ARIES Workshop on Electron-Cloud Effects 2018,* Elba, Italy, 2020, pp. 51–58.

[22] R. Valizadeh, O. B. Malyshev, S. Wang, S. A. Zolotovskaya, W. Allan Gillespie, and A. Abdolvand, "Low secondary electron yield engineered surface for electron cloud mitigation," Appl. Phys. Lett. **105**, 231605 (2014).

[23] D. Bajek, S. Wackerow, D. A. Zanin, L. Baudin, K. Bogdanowicz, E. G.-T. Valdivieso, S. Calatroni, B. Di Girolamo, M. Sitko, M. Himmerlich, M. Taborelli, P. Chiggiato, and A. Abdolvand, "Role of surface microgeometries on electron escape probability and secondary electron yield of metal surfaces," Sci. Rep. **10**, 250 (2020).

[24] P. Lorenz, M. Himmerlich, M. Ehrhardt, E. Bez, K. Bogdanowicz, M. Taborelli, and K. Zimmer, "Secondary electron yield reduction of copper after 355 nm ultrashort pulse laser ablation," Lasers Manuf. Mater. Process. **9**, 135–150 (2022).

[25] E. Bez, M. Himmerlich, P. Lorenz, M. Ehrhardt, A. G. Gunn, S. Pfeiffer, M. Rimoldi, M. Taborelli, K. Zimmer, P. Chiggiato, and A. Anders, "Influence of wavelength and accumulated fluence at picosecond laser-induced surface roughening of copper on secondary electron yield," J. Appl. Phys. **133**, 035303 (2023).

[26] S. Calatroni, E. Garcia-Tabares Valdivieso, H. Neupert, V. Nistor, A. T. Perez Fontenla, M. Taborelli, P. Chiggiato, O. Malyshev, R. Valizadeh, S. Wackerow, S. A. Zolotovskaya, W. A. Gillespie, and A. Abdolvand, "First accelerator test of vacuum components with laser-engineered surfaces for electron-cloud mitigation," Phys. Rev. Accel. Beams **20**, 113201 (2017).

[27] O. Aberle, I. B. Alonso, O. Brüning, P. Fessia, M. Lamont, L. Rossi, L. Tavian, and M. Zerlauth, "High-luminosity large hadron collider (HL-LHC): Technical design report V," *CERN Yellow Reports: Monographs*, CERN, 2020.

[28] L. Rosa, F. Melli, and L. Vincetti, "Analytical formulas for dispersion and effective area in hollow-core tube lattice fibers," Fibers **9**, 58 (2021).

[29] B. Debord, F. Amrani, L. Vincetti, F. Gérôme, and F. Benabid, "Hollow-core fiber technology: The rising of "gas photonics"," Fibers **7**, 16 (2019).

[30] E. P. Ippen, C. V. Shank, and T. K. Gustafson, "Self-phase modulation of picosecond pulses in optical fibers," Appl. Phys. Lett. **24**, 190–192 (2003).

[31] R. H. Stolen and C. Lin, "Self-phase-modulation in silica optical fibers," Phys. Rev. A **17**, 1448–1453 (1978).

[32] K.-H. Leitz, B. Redlingshöfer, Y. Reg, A. Otto, and M. Schmidt, "Metal ablation with short and ultrashort laser pulses," Phys. Procedia **12**, 230–238 (2011), lasers in Manufacturing 2011—Proceedings of the Sixth International WLT Conference on Lasers in Manufacturing.

[33] O. S. Brüning, P. Collier, P. Lebrun, S. Myers, R. Ostojic, J. Poole, and P. Proudlock, *LHC Design Report*, CERN Yellow Reports: Monographs (CERN, Geneva, 2004).

[34] J. Tagg, E. Bez, M. Himmerlich, and A. K. Reascos Portilla, "A reliable monitoring and control system for vacuum surface treatments", in *Proc. 18th Int. Conf. on Accelerator and Large Experimental Physics Control Systems (ICALEPCS)* Shanghai, China, 14.-22.10.2021, pp. 492–496, https://accelconf.web.cern.ch/icalepcs2021/.

[35] E. Malus, Baudouin, and J. B. Garnery, *Theorie de La Double Refraction de La Lumiere Dans Les Substances Cristallisees, Memoire Couronne Par l'institut Dans La Seance Publique Du 2 Janvier 1810, Par E. L. Malus.* (Garnery, libraire, rue de Seine, Holtel Mirabeau, 1810).

[36] P. J. Roberts, F. Couny, H. Sabert, B. J. Mangan, D. P. Williams, L. Farr, M. W. Mason, A. Tomlinson, T. A. Birks, J. C. Knight, and P. St J Russell, "Ultimate low loss of hollow-core photonic crystal fibres," Opt. Express **13**, 236–244 (2005).

[37] P. Lorenz, E. Bez, M. Himmerlich, M. Ehrhardt, M. Taborelli, and K. Zimmer, "Secondary electron yield engineering of copper surfaces by 532 nm ultrashort laser pulses," Procedia CIRP **111**, 662–666 (2022), 12th CIRP Conference on Photonic Technologies 2022.

[38] J. M. Liu, "Simple technique for measurements of pulsed Gaussian-beam spot sizes," Opt. Lett. **7**, 196–198 (1982).

[39] S. Calatroni, M. Arzeo, S. Aull, M. Himmerlich, P. Costa Pinto, W. Vollenberg, B. Di Girolamo, P. Cruikshank, P. Chiggiato, D. Bajek, S. Wackerow, and A. Abdolvand, "Cryogenic surface resistance of copper: Investigation of the impact of surface treatments for secondary electron yield reduction," Phys. Rev. Accel. Beams **22**, 063101 (2019).

[40] M. C. Biesinger, "Advanced analysis of copper x-ray photoelectron spectra," Surf. Interface Anal. **49**, 1325–1334 (2017).

[41] S. Poulston, P. M. Parlett, P. Stone, and M. Bowker, "Surface oxidation and reduction of CuO and Cu_2O studied using XPS and XAES," Surf. Interface Anal. **24**, 811–820 (1996).

[42] D. Tahir and S. Tougaard, "Electronic and optical properties of Cu, CuO and Cu_2O studied by electron spectroscopy," J. Phys.: Condens. Matter **24**, 175002 (2012).

[43] S. Calatroni, E. Garcia-Tabares Valdivieso, A. T. Perez Fontenla, M. Taborelli, H. Neupert, M. Himmerlich, P. Chiggiato, D. Bajek, S. Wackerow, and A. Abdolvand, "Optimization of the secondary electron yield of laser-structured copper surfaces at room and cryogenic temperature," Phys. Rev. Accel. Beams **23**, 033101 (2020).

[44] J. Ghijsen, L. H. Tjeng, J. van Elp, H. Eskes, J. Westerink, G. A. Sawatzky, and M. T. Czyzyk, "Electronic structure of Cu_2O and CuO," Phys. Rev. B **38**, 11322–11330 (1988).

[45] T. Schedel-Niedrig, T. Neisius, I. Böttger, E. Kitzelmann, G. Weinberg, D. Demuth, and R. Schlögl, "Copper (sub)oxide formation: A surface sensitive characterization of model catalysts," Phys. Chem. Chem. Phys. **2**, 2407–2417 (2000).

[46] V. Petit, M. Taborelli, H. Neupert, P. Chiggiato, and M. Belhaj, "Role of the different chemical components in the conditioning process of air exposed copper surfaces," Phys. Rev. Accel. Beams **22**, 083101 (2019).

[47] R. Cimino and I. Collins, "Vacuum chamber surface electronic properties influencing electron cloud phenomena," Appl. Surf. Sci. **235**, 231–235 (2004), 8th European Vacuum Conference and 2nd Annual Conference of the German Vacuum Society.

[48] F. Li, Z. Yang, Z. Lv, Y. Wang, Q. Li, Y. Wei, Y. Yang, X. Yang, and W. Zhao, "High energy femtosecond laser micromachining with hollow core photonic crystal fiber delivery," Optik **194**, 163093 (2019).